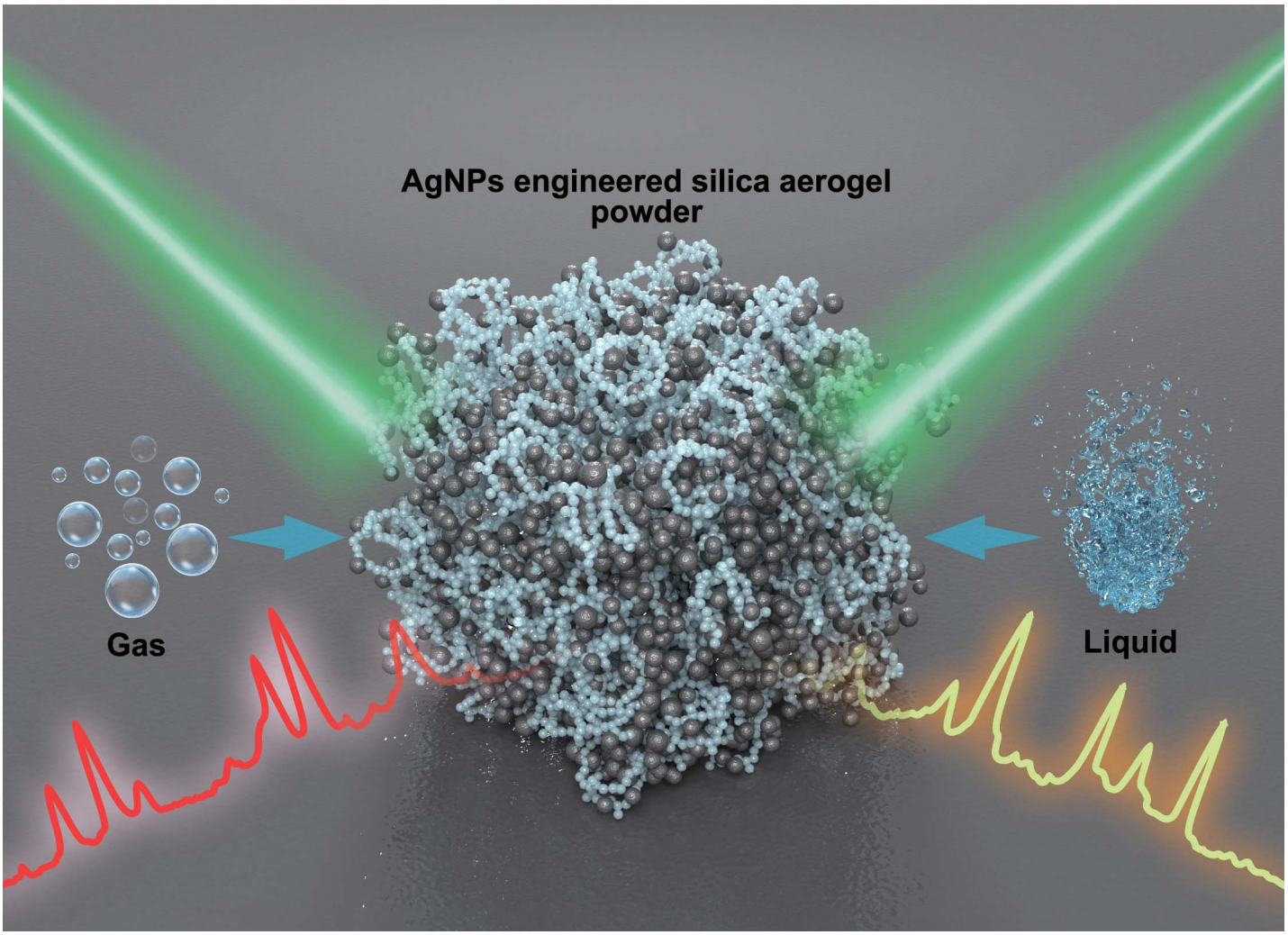

Showcasing research from Professor Zhipeng Li's laboratory, Department of Physics, Capital Normal University, Beijing, China.

Three-dimensional porous SERS powder for sensitive liquid and gas detections fabricated by engineering dense "hot spots" on silica aerogel

A three dimensional porous SERS powder material was developed in this study. Highly sensitive and homogeneous SERS detections on liquid and gas have been achieved, which demonstrates potential application for an artificial "nose".

As featured in:

See Zhipeng Li *et al.*, *Nanoscale Adv.*, 2021, **3**, 1012.

ROYAL SOCIETY OF CHEMISTRY

rsc.li/nanoscale-advances

Registered charity number: 207890

Nanoscale Advances

ROYAL SOCIETY OF CHEMISTRY

PAPER

View Article Online
View Journal | View Issue

Cite this: *Nanoscale Adv.*, 2021, **3**, 1012

Three-dimensional porous SERS powder for sensitive liquid and gas detections fabricated by engineering dense "hot spots" on silica aerogel†

Longkun Yang,[a] Zhifang Ren,[a] Meng Zhang,[a] Yanli Song,[a] Pan Li,[ab] Yun Qiu,[a] Pingye Deng[b] and Zhipeng Li *[a]

Received 11th October 2020
Accepted 30th November 2020

DOI: 10.1039/d0na00849d

rsc.li/nanoscale-advances

A three-dimensional porous SERS powder material, Ag nanoparticles-engineered-silica aerogel, was developed. Utilizing an *in situ* chemical reduction strategy, Ag nanoparticles were densely assembled on porous aerogel structures, thus forming three-dimensional "hot spots" distribution with intrinsic large specific surface area and high porosity. These features can effectively enrich the analytes on the metal surface and provide huge near field enhancement. Highly sensitive and homogeneous SERS detections were achieved not only on the conventional liquid analytes but also on gas with the enhancement factor up to ~10^8 and relative standard deviation as small as ~13%. Robust calibration curves were obtained from the SERS data, which demonstrates the potential for the quantification analysis. Moreover, the powder shows extraordinary SERS stability than the conventional Ag nanostructures, which makes long term storage and convenient usage feasible. With all of these advantages, the porous SERS powder material can be extended to on-site SERS "nose" applications such as liquid and gas detections for chemical analysis, environmental monitoring, and anti-terrorism.

Introduction

"Hot spots" generated by the surface plasmons coupling of neighboring metal nanostructures play a critical role in surface-enhanced Raman scattering (SERS).[1–4] Benefitting from the enormous local field, the SERS detection sensitivity can even reach a single-molecule level.[5–10] As is well known, the "hot spot" is small in size, and the enhancement ability is highly dependent on the random and complex light–substrate–analyte interactions. These intrinsic features always make the SERS enhancement irregular, which has been the main obstacle in the expansion of practical SERS applications, particularly for the on-site SERS detections.[11,12] Considerable efforts have been made to achieve SERS with high sensitivity and homogeneity. One feasible way is to largely increase the density of "hot spots" on SERS substrates. The irregularity of SERS can be well homogenized by the statistical average of multiple "hot spots". Various metal nanostructures have been rationally designed to increase the density of "hot spots" such as nanoparticle aggregates,[13–20] periodic arrays,[21–25] and mesostructures with roughened surfaces.[26,27] While, the nearly planar SERS substrates inevitably restrict the space density of "hot spots". Hence, three dimensional (3D) SERS active substrates have recently attracted great attention.[28–33] At present, two main technical routes have been reported to fabricate the 3D SERS substrates. One is to assemble the metallic nanostructures layer by layer at a liquid–liquid or liquid–air interface.[34–36] The other is to assemble/synthesize the nanoparticles directly on a 3D scaffold such as the butterfly wings,[37] metal–organic frameworks,[38] filter paper,[39] graphene foam,[40] and some hierarchical structures.[41–44] These 3D SERS substrates with a high density of "hot spots" in three dimensions, large surface area, and tolerance in focus misalignment have demonstrated considerable improvements in both sensitivity and homogeneity. Based on them, many studies have reported the construction of robust calibration curves from the SERS data, which advances the quantification analysis of SERS.[45–47] To fabricate 3D SERS substrates of high quality, it is critical to select proper scaffold materials and engineer dense "hot spots" on templates. Porous silica aerogel with high porosity (~99%), large specific surface area (~1000 $m^2 g^{-1}$), and especially high optical transparency (~99%) in the visible region can be an ideal scaffold material.[48,49] However, the average pore size is only tens of nanometers. There is still a lack of effective methods to "build" metallic nanostructures in such small pores.

In this paper, a facile *in situ* reducing method was developed to synthesize Ag nanoparticles on porous silica aerogel scaffold to form a 3D SERS powder material. The obtained Ag

[a]*The Beijing Key Laboratory for Nano-Photonics and Nano-Structure (NPNS), Department of Physics, Capital Normal University, Beijing 100048, P. R. China. E-mail: zpli@cnu.edu.cn*

[b]*Beijing Center for Physical and Chemical Analysis, Beijing Academy of Science and Technology, Beijing 100089, P. R. China*

† Electronic supplementary information (ESI) available. See DOI: 10.1039/d0na00849d

nanoparticles-engineered-silica aerogel (AgNPs-SA) powder has a large specific surface area (~17 times larger than the conventional AgNPs aggregates) and dense Ag nanoparticles distribution on and inside the porous structure. We applied it for both liquid and gaseous SERS detections. Due to the unique structural characteristics, this 3D SERS powder material demonstrated high sensitivity and homogeneity, with an enhancement factor as high as $\sim 10^8$ and relative standard deviation as small as ~13%. Robust SERS calibration curves have been achieved over wide concentration ranges. Furthermore, we demonstrated that the porous AgNPs-SA powder has higher SERS stability than the conventional AgNPs aggregates, which would be convenient for storage and usage, thereby facilitating on-site SERS "nose" applications.

Methods

Materials

All chemical reagents were purchased from Sigma-Aldrich, including silver nitrate ($AgNO_3$, 99%), sodium citrate (99%), rhodamine 6G (R6G, 95%), 4-aminothiophenol (4-ATP, 97%), melamine (99%), thiram (analytical standard), and pyridine (99%). The hydrophilic silica aerogel was purchased from Guangdong Alison Hi-Tech Co., Ltd.

Preparation of the Ag nanoparticles-engineered-porous silica aerogel

The bulky aerogel was ground to a powder before use. Firstly, the reactant solution was prepared by mixing 15 ml $AgNO_3$ (20 mM) and 15 ml sodium citrate (4 mM). Then, the silica aerogel powder (15 mg) was added to the mixture. It was clearly seen that the silica aerogel could soak the reagent like a sponge because of the porous structure. After stirring for 10 min, the reactant mixture was heated to 100 °C. Then, the solution turned into a light green color, which indicated the formation of silver nanoparticles. The reaction was then continued for the next 20 min, and the silver nanoparticles grew directly on and inside the silica aerogel. Finally, the Ag nanoparticles-engineered-silica aerogel was formed and precipitated at the bottom. The sediment was washed by water two times and dried in ambient conditions for use.

Characterizations

The surface morphology and elemental compositions were characterized by a scanning electron microscope on a Hitachi S4800 equipped with an energy-dispersive X-ray spectrometer. The surface area and pore properties of the silica aerogel and AgNPs-SA were determined from nitrogen adsorption–desorption experiments at 77.3 K using an accelerated surface area and porosity system (ASAP 2460, Micromeritics instrument Ltd., USA). The specific surface area was determined by a multipoint Brunauer–Emmett–Teller (BET) method using the adsorption data. The desorption isotherm was used to determine the pore size distribution and cumulative pore volume using the Barrett–Joyner–Halenda (BJH) method. The UV-Vis spectrum was measured using a SHIMADZU UV-Vis spectrophotometer in the wavelength range from 300 to 900 nm. The SERS measurements were performed on inVia Renishaw Raman Spectrometer using a 50× objective lens (N.A. = 0.5) and 532 nm as the excitation wavelength. The excitation power was about 70 μW, and the integration time was 10 s, if not stated otherwise.

Results and discussion

Fig. 1a shows the scanning electron microscope (SEM) image of a typical micro-size silica aerogel particle. The magnified view in the inset clearly demonstrates its porous structure. The synthesized AgNPs-SA structure is presented in Fig. 1b. The Ag nanoparticles with an average diameter of about 50 nm grow densely on the surface of the silica aerogel. The energy-dispersive X-ray spectroscopy (EDS) elemental mappings of Si and Ag (Fig. 1c and d) can reconstruct the morphology of particles in Fig. 1b, which confirms the formation of the AgNPs-SA composite. Additionally, we reported that the size and coverage of Ag nanoparticles on the aerogel scaffold were highly dependent on the $AgNO_3$ concentration, as shown in Fig. S1.† It is demonstrated that 20 mM silver nitrate and 4 mM sodium citrate can be the optimum condition for AgNPs-SA synthesis, with Ag nanoparticles densely and uniformly distributed on the aerogel scaffold, which facilitates the SERS measurements. Here, note that the silica aerogel particles were first thoroughly soaked with chemical reagents, and then the reduction process was triggered. Hence, it can be expected that the Ag nanoparticles can effectively grow in the bulk of silica aerogel. This can be confirmed by cross-sectional SEM images (Fig. S2†) and EDS mapping analysis (Fig. S3†), where we cut open the AgNPs-SA particle by a micromanipulator. The results clearly demonstrate that the Ag nanoparticles can densely spread on both the external surface and inside the aerogel, thus forming a 3D structure.

Utilizing nitrogen adsorption–desorption measurements, the specific surface area, pore size, and cumulative pore volume of silica aerogel, collapsed-aerogel, AgNPs-SA, and AgNPs aggregates were investigated, which are summarized in Table 1 (see ESI† for the details of AgNPs aggregates preparation). It is well known that the porous structure of silica aerogel has a tendency to collapse during the drying process because of the capillary force. Consequently, the surface area slightly reduces from 502 to 482 $m^2\ g^{-1}$, followed by a significant reduction in the pore diameter (from 27 to 8 nm) and cumulative pore volume (from 3.3 to 1.0 $m^3\ g^{-1}$). However, for AgNPs-SA, the specific surface area and cumulative pore volume decreased further to 123 $m^2\ g^{-1}$ and 0.35 $m^3\ g^{-1}$, though the corresponding average pore diameter was almost the same as the collapsed-aerogel. This can be understood by the fact that the pores will be filled with massive Ag nanoparticles during the reduction process, which thus dramatically decreases the surface area and pore volume. Here, note that the specific surface area of AgNPs-SA was still much larger than that of the conventional AgNPs aggregate (7 $m^2\ g^{-1}$). Thus, it can be expected that these porous AgNPs-SA powder would provide much more active sites for the adsorption of analyte molecules than the conventional AgNPs aggregate.

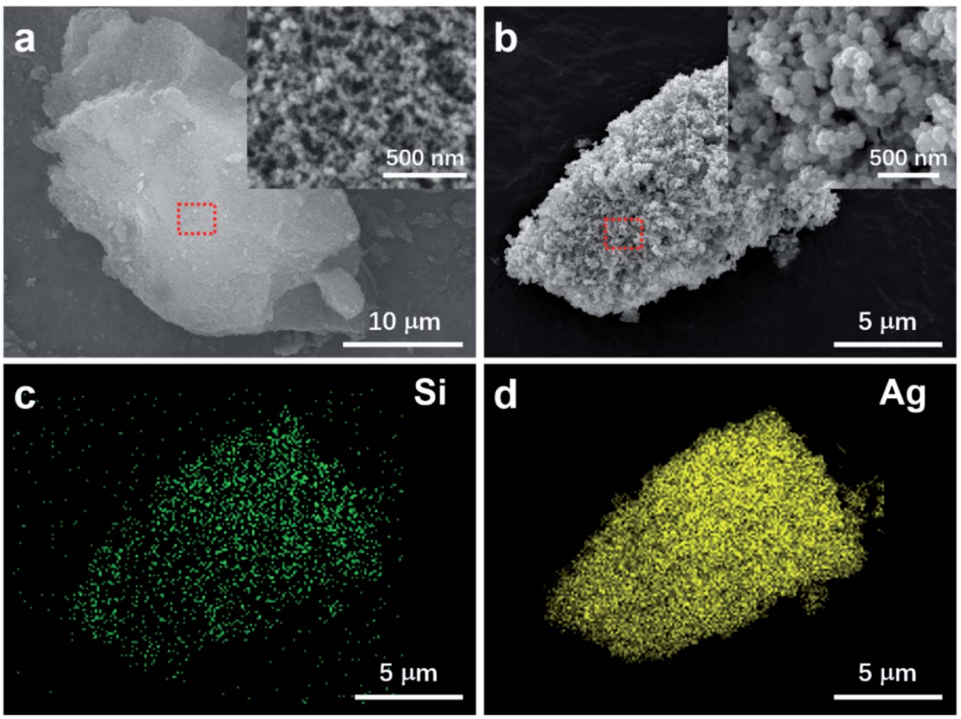

Fig. 1 The surface morphology and elemental analysis of the AgNPs-SA powder. (a) The SEM image of the silica aerogel particle. The inset shows the corresponding magnified image. (b) The surface morphology of the synthesized AgNPs-SA. The inset shows the corresponding magnified image. (c) and (d) The elemental mappings of AgNPs-SA composite in (b) by using Si and Ag, respectively.

The SERS performance of this porous AgNPs-SA substrate was then evaluated using R6G as a Raman probing molecule. According to the UV-Vis extinction spectrum of the AgNPs-SA powder (Fig. S5†), broadband with a peak at around 510 nm was observed. Hence, the 532 nm laser was selected for the SERS excitation. In experiments, a certain amount of the AgNPs-SA powder (3 mg) was added into 10 ml of R6G solution (1.0×10^{-10} M), which was then and left undisturbed for about 4 h at 4 °C. Then, the precipitate was dropped on the Si slice and dried under ambient conditions for use. The SERS spectra of R6G were acquired from randomly selected 30 spots on different AgNPs-SA particles. As shown in Fig. 2a, these spectra demonstrate superior consistency with each other, and the Raman fingerprints of R6G can be clearly identified at 1648 cm^{-1}, 1573 cm^{-1}, 1509 cm^{-1}, 1362 cm^{-1}, and 1309 cm^{-1}. Fig. 2b shows the histogram of the SERS intensity at 1362 cm^{-1} (C–C stretching of the aromatic ring). The SERS enhancement factor (EF) was then estimated by the equation as follows:[50–53]

$$EF = \frac{I_{SERS}}{I_{Bulk}} \times \frac{N_{Bulk}}{N_{SERS}}, \quad (1)$$

where I_{SERS} and I_{Bulk} are the intensity of a Raman mode with and without the surface enhancement, respectively. N_{SERS} and N_{Bulk} refer to the number of R6G molecules contributing to the SERS and Raman scattering, respectively. By selecting the R6G band at 1362 cm^{-1} as a reference, the SERS EF of the 3D AgNPs-SA was estimated to be $\sim 1.0 \times 10^{8}$ (see ESI† for details). Here, the EF is an average value over the whole laser-substrate interaction space, and the enhancement from a single "hot spot" of nanoaggregates could be much larger. Furthermore, we noticed that the relative standard deviation (RSD) of $I_{1362\ cm^{-1}}$ could be as small as ~13% for the SERS acquired from randomly selected 30 spots on different AgNPs-SA particles. If the spectra were measured from one AgNPs-SA particle, the RSD can even lower down up to 7% (Fig. S7†), which indicates the excellent SERS homogeneity.

We further verified the calibrated SERS of AgNPs-SA at different concentrations ranging from 10^{-8} to 10^{-12} M. At each

Table 1 The specific surface area, average pore size, and cumulative pore volume of silica aerogel, collapsed-aerogel, AgNPs-SA, and AgNPs aggregates, based on nitrogen adsorption–desorption measurements (Fig. S4)

	Silica aerogel	Collapsed-aerogel	AgNPs-SA	AgNPs aggregates
Specific surface area	502 $m^2\ g^{-1}$	482 $m^2\ g^{-1}$	123 $m^2\ g^{-1}$	7 $m^2\ g^{-1}$
Average pore size	27 nm	8 nm	10 nm	—
Cumulative pore volume	3.3 $m^3\ g^{-1}$	1.0 $m^3\ g^{-1}$	0.35 $m^3\ g^{-1}$	—

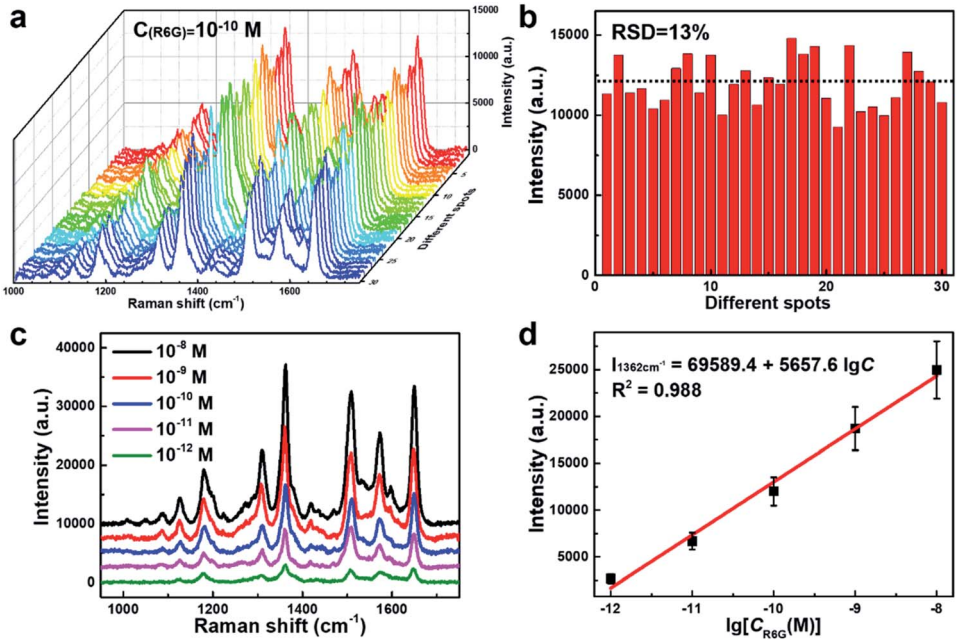

Fig. 2 The SERS detection on liquid R6G solution. (a) The SERS spectra of R6G measured at 10^{-10} M. 30 spots on different AgNPs-SA particles were randomly selected to acquire the spectra. (b) The statistics of SERS intensity at 1362 cm^{-1}. (c) The SERS spectra of R6G at different concentrations (10^{-8} to 10^{-12} M). (d) The SERS intensity at 1362 cm^{-1} as a function of R6G logarithmic concentrations. The error bars indicate the standard deviations of SERS measurements at the randomly selected spots. The red curve presents the corresponding linear fitting line.

concentration, the SERS spectra of R6G were acquired by randomly selecting 30 spots on different AgNPs-SA particles (Fig. S8†). The representative SERS spectra are shown in Fig. 2c. Most of the Raman fingerprints of R6G, such as 1648 cm^{-1}, 1509 cm^{-1}, and 1362 cm^{-1}, can still be clearly distinguished even at a concentration as low as 10^{-12} M. Fig. 2d shows the average SERS intensity ($I_{1362\ cm^{-1}}$) *versus* the logarithms of R6G concentration. Interestingly, a robust linear relationship was obtained, with the fitting correlation coefficient $R^2 = 0.988$. This wide linear response benefits from the unique structural characteristics of the AgNPs-SA powder. First, the closely packed nanoparticles on and inside the porous silica aerogel would greatly increase the density of "hot spots" in the 3D space such that the intensity fluctuation during the measurements can be suppressed to a large extent. Second, the specific surface area of the AgNPs-SA powder was ~17 times larger than that of the conventional AgNPs aggregates, where more molecules would be adsorbed. The ultra-trace detections of melamine and thiram in the liquid using this unique AgNPs-SA powder were validated and are shown in the ESI (Fig. S9†).

So far, the gas-phase SERS detection remains extremely challenging due to the low affinity of airborne species to the metal surface.[54–58] Our porous AgNPs-SA powder with a high density of "hot spots" and large specific surface area would be an ideal solution for the gas-phase SERS detections. Here, we utilized porous AgNPs-SA to detect gaseous 4-ATP, which is an inhalation noxious. To produce gas-phase 4-ATP molecules, a certain amount of 4-ATP solution in alcohol was heated at 50 °C inside an airtight oven (total volume ~27 L). Furthermore, the AgNPs-SA powder was left in the oven for 4 h to reach the adsorption equilibrium of gas-phase 4-ATP. After that, the powder was collected in a cuvette for further SERS measurements. Moreover, 30 spectra were measured at each concentration (Fig. S10†). Fig. 3a shows the representative SERS spectra of 4-ATP at different concentrations ranging from 0.05 to 1 ppm. Raman fingerprints at 1576 cm^{-1}, 1436 cm^{-1}, 1389 cm^{-1}, 1141 cm^{-1}, and 1075 cm^{-1} can be clearly identified even at 0.05 ppm. Such ultrasensitive and reliable gaseous detections demonstrate the unique advantages of the porous AgNPs-SA powder over the conventional Ag aggregates.

Subsequently, the strongest characteristic peak at 1436 cm^{-1} was selected to plot the calibrated SERS curves *versus* the 4-ATP concentrations, as shown in Fig. 3b. It was found that the SERS intensities were almost linear at low concentrations (0.05–0.25 ppm). However, at higher concentrations (>0.25 ppm), an obvious plateau region was observed, indicating that the adsorption of 4-ATP onto the AgNPs-SA has reached the saturation level. To understand the interaction of 4-ATP with the silver surface, the experimental data were fitted using the Hill equation.[58–60] Averagely, it is reasonable to assume that the SERS intensity (I_{SERS}) is proportional to the surface coverage (Θ) of adsorbed molecules on the AgNPs-SA surface. The surface coverage (Θ) can be described by the Hill equation. Then, I_{SERS} can be expressed as:

$$I_{SERS} = I_0 \times \Theta = I_0 \frac{1}{1 + \left(\frac{K_A}{C}\right)^n}, \quad (2)$$

where I_0 is the SERS intensity at the saturated coverage $\Theta = 1$, C is the concentration of 4-ATP molecules, n is the Hill coefficient,

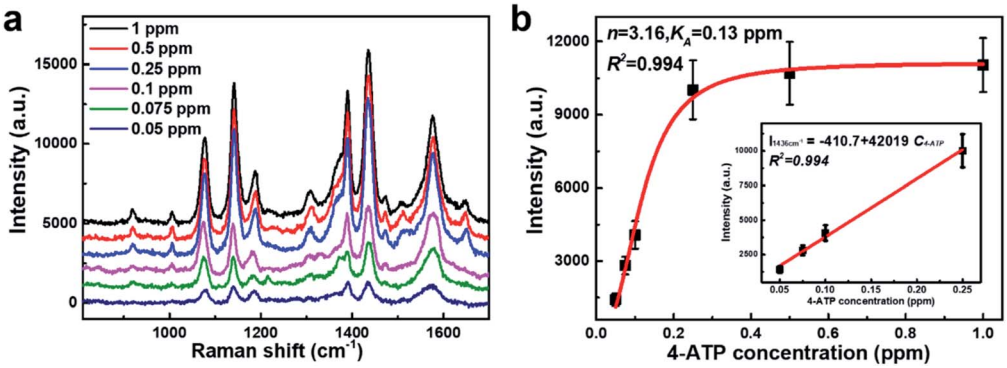

Fig. 3 The SERS of gaseous 4-ATP molecules. (a) The SERS spectra showing the increasing concentration of gaseous 4-ATP from 0.05 to 1 ppm. (b) Calibration measurements as the function of gaseous 4-ATP concentrations. Black squares: the experimental SERS intensity at 1436 cm^{-1}. Red curve: fitting by the Hill model. The inset shows the linear fitting of $I_{1436\ cm^{-1}}$ *versus* the concentrations of gaseous 4-ATP (0.05–0.25 ppm). The error bars indicate the standard deviations of SERS measurements at randomly selected spots.

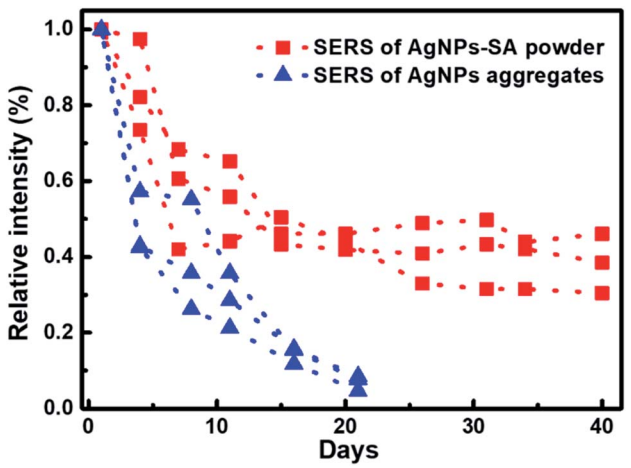

Fig. 4 SERS stability of the AgNPs-SA powder. Squares and triangles demonstrate the SERS intensity ($I_{1436\ cm^{-1}}$ of 4-ATP) evolutions of 3D AgNPs-SA powder and conventional 2D AgNPs aggregates with different preserved time in ambient condition, respectively. For comparison, three groups of controlled experiments were done. The dash lines are plotted to guide eyes.

and K_A is the concentration of molecules producing half coverage. As shown in Fig. 3b, the fitting curve agrees well with the experimental results ($R^2 = 0.994$), where we can extract the key parameters: $n = 3.16$ and $K_A = 0.13$ ppm. Here, $n > 1$ indicates the positive cooperativity with respect to 4-ATP binding to the silver surface.[60,61] The relatively small value of K_A (0.13 ppm) further confirms the high affinity of 4-ATP towards the silver surface.[58,61] It also implies that the AgNPs-SA powder was so sensitive that only 5% coverage of 4-ATP would be enough for an effective detection (for the calculation of 4-ATP coverage, see ESI†). Moreover, at low concentrations (0.05–0.25 ppm), a linear relationship between $I_{1436\ cm^{-1}}$ and 4-ATP concentrations was obtained (inset of Fig. 3b), which demonstrates the potential of this porous AgNPs-SA powder for the gaseous quantification analysis. Furthermore, the gaseous pyridine with inhalation toxicity was effectively detected at concentrations ranging from 0.1 to 1.5 ppm (Fig. S11†). The main Raman peaks at 624 cm^{-1}, 1035 cm^{-1}, and 1599 cm^{-1} can be clearly observed even at 0.1 ppm (far below the safety limit of 5 ppm set by the Material Safety Data Sheet). The intensity of 1035 cm^{-1} mode can be fitted by the Hill equation as well, with $n = 1.7$ and $K_A = 0.23$ ppm.

The stability of SERS substrates in ambient conditions is another major concern for practical applications. The key to enhancing stability was to prevent silver metal nanostructures from oxidation in the air.[62] Herein, we monitored the temporal evolution of the 4-ATP SERS intensity (10^{-10} M) with AgNPs-SA powder preserved in the air. Three independent groups of the data are shown by the red squares in Fig. 4. We found that the SERS enhancement of the AgNPs-SA powder dramatically decreased in the first 7 days, which can be explained by the inevitable activity loss of Ag nanoparticles on the external surface when exposed to air. Then, in the following four weeks, the drop in the SERS enhancement slowed down and gradually reached an equilibrium state. Averagely, 40% of the enhancement ability can still be retained after 40 days' exposure to air. For comparison, the SERS performance of the conventional AgNPs aggregates under the same experimental conditions was studied. To make the SERS data comparable with that obtained from the aerogel-silver structure, only the aggregates with a size larger than laser spot (>2 μm) were measured. As shown by blue triangles, the enhancement decreased rapidly with time. After three weeks' exposure to air, only 10% of the enhancement was reserved. Obviously, the SERS of our porous AgNPs-SA powder was much more stable than that of the conventional AgNPs aggregates. It seems that the nanoporous structure of the AgNPs-SA powder plays a key role in preventing or slowing the oxidation of silver nanoparticles inside the silica aerogel,[63] which is important for future studies.

Conclusions

In summary, we developed a facile *in situ* reduction method to synthesize silver nanoparticles in and on porous silica aerogel. The obtained AgNPs-SA powder can be an ideal 3D SERS

material, possessing dense "hot spots" in three dimensions, large specific surface area, and high porosity. Benefiting from the unique structural characteristics, highly sensitive and homogeneous SERS detections on liquid R6G and gaseous 4-ATP were achieved, with the EF up to $\sim 10^8$ and RSD as small as ~13%. Well and wide calibration SERS curves were obtained, which demonstrates the promising potential for the quantification analysis. Moreover, AgNPs-SA showed extraordinary SERS stability in air. Unlike the conventional SERS substrate, this stable AgNPs-SA existing in the form of porous powder would be quite convenient for the storage and usage, thereby facilitating on-site SERS "nose" applications such as quick and reliable liquid/gas detection for the chemical analysis, food safety inspections, and anti-terrorism.

Conflicts of interest

There are no conflicts to declare.

Acknowledgements

This work was supported by the National Natural Science Foundation of China (Grant No. 11704266 and 11774245), the Fok Ying Tung Education Foundation, China (Grant No. 151010), the General Foundation of Beijing Municipal Commission of Education (Grant No. KM201810028006), the Beijing Natural Science Foundation (Z190006), the National Program for Support of Top-notch Young Professional, the Training Program of the Major Research Plan of Capital Normal University, Yanjing Scholar Foundation of Capital Normal University, the Scientific Research Base Development Program of Beijing Municipal Commission of Education and the Beijing Key Laboratory of Metamaterials and Devices.

Notes and references

1 N. J. Halas, S. Lal, W. Chang, S. Link and P. Nordlander, *Chem. Rev.*, 2011, **111**, 3913–3961.
2 J. Nam, J. Oh, H. Lee and Y. D. Suh, *Acc. Chem. Res.*, 2016, **49**, 2746–2755.
3 S. Ding, E. You, Z. Tian and M. Moskovits, *Chem. Soc. Rev.*, 2017, **46**, 4042–4076.
4 D. M. Solís, J. M. Taboada, F. Obelleiro, L. M. Liz-Marzán and F. J. García de Abajo, *ACS Nano*, 2014, **8**, 7559–7570.
5 E. C. L. Ru and P. G. Etchegoin, *Annu. Rev. Phys. Chem.*, 2012, **63**, 65–87.
6 H. Xu, E. J. Bjerneld, M. Käll and L. Börjesson, *Phys. Rev. Lett.*, 1999, **83**, 4357–4360.
7 D. Lim, K. S. Jeon, H. M. Kim, J. Nam and Y. D. Suh, *Nat. Mater.*, 2010, **9**, 60–67.
8 S. Yang, X. Dai, B. B. Stogin and T. S. Wong, *Proc. Natl. Acad. Sci. U. S. A.*, 2016, **113**, 268–273.
9 F. Benz, M. K. Schmidt, A. Dreismann, R. Chikkaraddy, Y. Zhang, A. Demetriadou, C. Carnegie, H. Ohadi, B. de Nijs, R. Esteban, J. Aizpurua and J. J. Baumberg, *Science*, 2016, **354**, 726–729.
10 A. B. Zrimsek, N. Chiang, M. Mattei, S. Zaleski, M. O. Mcanally, C. T. Chapman, A.-I. Henry, G. C. Schatz and R. P. Van Duyne, *Chem. Rev.*, 2017, **117**, 7583–7613.
11 R. Panneerselvam, G. Liu, Y. Wang, J. Liu, S. Ding, J. Li, D. Wu and Z. Tian, *Chem. Commun.*, 2018, **54**, 10–25.
12 A. I. Pérez-Jiménez, D. Lyu, Z. Lu, G. Liu and B. Ren, *Chem. Sci.*, 2020, **11**, 4563–4577.
13 J. Huang, L. Zhang, B. Chen, N. Ji, F. Chen, Y. Zhang and Z. Zhang, *Nanoscale*, 2010, **2**, 2733–2738.
14 H. Kang, S. Jeong, Y. Park, J. Yim, B. Jun, S. Kyeong, J. Yang, G. Kim, S. Hong, L. P. Lee, J. Kim, H. Lee, D. Jeong and Y. Lee, *Adv. Funct. Mater.*, 2013, **23**, 3719–3727.
15 H. Liu, X. Zhang, T. Zhai, T. Sander, L. Chen and P. J. Klar, *Nanoscale*, 2014, **6**, 5099–5105.
16 S. Tian, O. Neumann, M. J. McClain, X. Yang, L. Zhou, C. Zhang, P. Nordlander and N. J. Halas, *Nano Lett.*, 2017, **17**, 5071–5077.
17 H. Tian, N. Zhang, L. Tong and J. Zhang, *Small Methods*, 2017, **1**, 1700126.
18 Q. Chen, Y. Fu, W. Zhang, S. Ye, H. Zhang, F. Xie, L. Gong, Z. Wei, H. Jin and J. Chen, *Talanta*, 2017, **165**, 516–521.
19 D. Renard, S. Tian, A. Ahmadivand, C. J. DeSantis, B. D. Clark, P. Nordlander and N. J. Halas, *ACS Nano*, 2019, **13**, 3117–3124.
20 D. Sun, G. Qi, S. Xu and W. Xu, *RSC Adv.*, 2016, **6**, 53800–53803.
21 D. Choi, Y. Choi, S. Hong, T. Kang and L. P. Lee, *Small*, 2010, **6**, 1741–1744.
22 M. P. Cecchini, V. A. Turek, J. Paget, A. A. Kornyshev and J. B. Edel, *Nat. Mater.*, 2013, **12**, 165–171.
23 H. Chen, M. Lin, C. Wang, Y. Chang and S. Gwo, *J. Am. Chem. Soc.*, 2015, **137**, 13698–13705.
24 X. Hou, Q. Wang, G. Mao, H. Liu, R. Yu and X. Ren, *Appl. Surf. Sci.*, 2018, **437**, 92–97.
25 J. Meng, X. Tang, B. Zhou, Q. Xie and L. Yang, *Talanta*, 2017, **164**, 693–699.
26 J. Fang, S. Du, S. Lebedkin, Z. Li, R. Kruk, M. M. Kappes and H. Hahn, *Nano Lett.*, 2010, **10**, 5006–5013.
27 Z. Liu, F. Zhang, Z. Yang, H. You, C. Tian, Z. Li and J. Fang, *J. Mater. Chem. C*, 2013, **1**, 5567–5576.
28 H. Liu, Z. Yang, L. Meng, Y. Sun, J. Wang, L. Yang, J. Liu and Z. Tian, *J. Am. Chem. Soc.*, 2014, **136**, 5332–5341.
29 M. Tabatabaei, M. Najiminaini, K. Davieau, B. Kaminska, M. R. Singh, J. J. L. Carson and F. Lagugné-Labarthet, *ACS Photonics*, 2015, **2**, 752–759.
30 Z. Li, S. Jiang, Y. Huo, T. Ning, A. Liu, C. Zhang, Y. He, M. Wang, C. Li and B. Man, *Nanoscale*, 2018, **10**, 5897–5905.
31 J. Quan, J. Zhang, J. Li, X. Zhang, M. Wang, N. Wang and Y. Zhu, *Carbon*, 2019, **147**, 105–111.
32 Z. Yang, L. Meng, J. Lin, W. Yang, P. Radjenovic, S. Shen, Q. Xu, Z. Yang, Z. Tian and J. Li, *Adv. Opt. Mater.*, 2019, **7**, 1901010.
33 C. Zhang, C. Li, J. Yu, S. Jiang, S. Xu, C. Yang, Y. Liu, X. Gao, A. Liu and B. Man, *Sens. Actuators, B*, 2018, **258**, 163–171.
34 C. Hamon, S. M. Novikov, L. Scarabelli, D. M. Solís, T. Altantzis, S. Bals, J. M. Taboada, F. Obelleiro and L. M. Liz-Marzán, *ACS Photonics*, 2015, **2**, 1482–1488.

35 P. Li, Y. Li, Z. Zhou, S. Tang, X. Yu, S. Xiao, Z. Wu, Q. Xiao, Y. Zhao, H. Wang and P. K. Chu, *Adv. Mater.*, 2016, **28**, 2511–2517.
36 Y. Zhang, S. Chen, P. Radjenovic, N. Bodappa, H. Zhang, Z. Yang, Z. Tian and J. Li, *Anal. Chem.*, 2019, **91**, 5316–5322.
37 L. Wu, W. Wang, W. Zhang, H. Su, Q. Liu, J. Gu, T. Deng and D. Zhang, *NPG Asia Mater.*, 2018, **10**, e462.
38 Y. Hu, J. Liao, D. Wang and G. Li, *Anal. Chem.*, 2014, **86**, 3955–3963.
39 Y. H. Ngo, D. Li, G. P. Simon and G. Garnier, *Langmuir*, 2012, **28**, 8782–8790.
40 C. Srichan, M. Ekpanyapong, M. Horprathum, P. Eiamchai, N. Nuntawong, D. Phokharatkul, P. Danvirutai, E. Bohez, A. Wisitsoraat and A. Tuantranont, *Sci. Rep.*, 2016, **6**, 23733.
41 J. Huang, D. Ma, F. Chen, M. Bai, K. Xu and Y. Zhao, *Anal. Chem.*, 2015, **87**, 10527–10534.
42 M. Lee, T. Y. Jeon, C. Mun, J. Kwon, J. Yun, S. Kim, D. Kim, S. Chang and S. Park, *RSC Adv.*, 2017, **7**, 17898–17905.
43 M. Lafuente, E. J. W. Berenschot, R. M. Tiggelaar, R. Mallada, N. R. Tas and M. P. Pina, *Micromachines*, 2018, **9**, 60.
44 X. Zhao, M. Deng, G. Rao, Y. Yan, C. Wu, Y. Jiao, A. Deng, C. Yan, J. Huang, S. Wu, W. Chen, T. Lei, P. Xu, W. He and J. Xiong, *Small*, 2018, **14**, 1802477.
45 L. Tian, M. Su, F. Yu, Y. Xu, X. Li, L. Li, H. Liu and W. Tan, *Nat. Commun.*, 2018, **9**, 3642.
46 Y. Li, R. Lu, J. Shen, W. Han, X. Sun, J. Li and L. Wang, *Analyst*, 2017, **142**, 4756–4764.
47 Z. Li, G. Meng, Q. Huang, X. Hu, X. He, H. Tang, Z. Wang and F. Li, *Small*, 2015, **11**, 5452–5459.
48 A. S. Dorcheh and M. H. Abbasi, *J. Mater. Process. Technol.*, 2008, **199**, 10–26.
49 J. L. Gurav, I. Jung, H. Park, E. S. Kang and D. Y. Nadargi, *J. Nanomater.*, 2010, **2010**, 409310.
50 B. Xu, Z. Ma, L. Wang, R. Zhang, L. Niu, Z. Yang, Y. Zhang, W. Zheng, B. Zhao, Y. Xu, Q. Chen, H. Xia and H. Sun, *Chem. Sci.*, 2011, **11**, 3347–3351.
51 Q. Guo, M. Xu, Y. Yuan, R. Gu and J. Yao, *Langmuir*, 2016, **32**, 4530–4537.
52 H. Lu, L. Zhu, C. Zhang, K. Chen and Y. Cui, *Anal. Chem.*, 2018, **90**, 4535–4543.
53 S. M. Novikov, S. Boroviks, A. B. Evlyukhin, D. E. Tatarkin, A. V. Arsenin, V. S. Volkov and S. I. Bozhevolnyi, *ACS Photonics*, 2020, **7**, 1708–1715.
54 L. E. Kreno, N. G. Greeneltch, O. K. Farha, J. T. Hupp and R. P. Van Duyne, *Analyst*, 2014, **139**, 4073–4080.
55 Y. Xie, X. Wang, X. Han, X. Xue, W. Ji, Z. Qi, J. Liu, B. Zhao and Y. Ozaki, *Analyst*, 2010, **135**, 1389–1394.
56 C. Qian, Q. Guo, M. Xu, Y. Yuan and J. Yao, *RSC Adv.*, 2015, **5**, 53306–53312.
57 G. C. Phan-Quang, H. K. Lee, H. W. Teng, C. S. L. Koh, B. Q. Yim, E. K. M. Tan, W. L. Tok, I. Y. Phang and X. Y. Ling, *Angew. Chem., Int. Ed.*, 2018, **57**, 5792–5796.
58 S. Kim, D. Kim and S. Park, *Analyst*, 2018, **143**, 3006–3010.
59 A. Kim, S. J. Barcelo and Z. Li, *Nanotechnol*, 2015, **26**, 015502.
60 A. Hill, *J. Physiol.*, 1910, **40**, 1–7.
61 Y. Huang, D. Wu, H. Zhu, L. Zhao, G. Liu, B. Ren and Z. Tian, *Phys. Chem. Chem. Phys.*, 2012, **14**, 8485–8497.
62 L. Ma, Y. Huang, M. Hou, Z. Xie and Z. Zhang, *Sci. Rep.*, 2015, **5**, 12890.
63 D. Mu, Z. Liu, C. Huang and N. Djilali, *Microfluid. Nanofluid.*, 2008, **4**, 257–260.